A feasibility study for simultaneous measurements of water vapor and precipitation parameters using a three-frequency radar

R. Meneghini[1], L. Liao[2], L. Tian[3]

1. Microwave Sensors Branch, Code 975, NASA/GSFC, Greenbelt, MD 20771
2. Goddard Earth Sciences and Technology/Caelum, Greenbelt, MD
3. Goddard Earth Sciences and Technology/University of MD, Baltimore MD

Abstract

The radar return powers from a three-frequency radar, with center frequency at 22.235 GHz and upper and lower frequencies chosen with equal water vapor absorption coefficients, can be used to estimate water vapor density and parameters of the precipitation. A linear combination of differential measurements between the center and lower frequencies on one hand and the upper and lower frequencies on the other provide an estimate of differential water vapor absorption. The coupling between the precipitation and water vapor estimates is generally weak but increases with bandwidth and the amount of non-Rayleigh scattering of the hydrometeors. The coupling leads to biases in the estimates of water vapor absorption that are related primarily to the phase state and the median mass diameter of the hydrometeors. For a down-looking radar, path-averaged estimates of water vapor absorption are possible under rain-free as well as raining conditions by using the surface returns at the three frequencies. Simulations of the water vapor attenuation retrieval show that the largest source of error typically arises from the variance in the measured radar return powers. Although the error can be mitigated by a combination of a high pulse repetition frequency, pulse compression, and averaging in range and time, the radar receiver must be stable over the averaging period. For fractional bandwidths of 20% or less, the potential exists for simultaneous measurements at the three frequencies with a single antenna and transceiver, thereby significantly reducing the cost and mass of the system.

1. Introduction

Many remote sensing techniques are being used experimentally or operationally to estimate atmospheric water vapor. These include radiometers at microwave [Westwater and Han, 2001; Solheim et al., 1998; Schultz et al., 1993; Schlussel and Bauer, 1993], millimeter wave [Rosenkranz, 2001; Wang et al., 1995; Wilheit, 1990] and IR [Schmetz and Turpeinen, 1998; Hagen et al., 2004]; Raman and differential absorption (DIAL) lidars [Whiteman, 2003; Behrendt et al., 2002; Brassington, 1982]; and GPS-based techniques [Bevis et al., 1992; Alber et al., 1997]. With a few possible exceptions [e.g., Liljegren, 2004] most of the instruments and retrieval methods are not applicable in the presence of rain.

Although little work seems to have been done on water vapor estimation using radar, an exception is the work of Tian et al. (2004) who have analyzed dual-frequency (10 and 94 GHz) airborne Doppler radar data. By deriving the hydrometeor size distribution from the Doppler velocities and then modifying the radar reflectivity factors, Z, to account for Mie scattering and attenuation effects, the attenuation from cloud and gases can be inferred from the difference in the modified Z values at the two frequencies. In this paper, a three-frequency radar is studied where one of the frequencies is taken at the 22.235 GHz line center with the others chosen at a lower and higher frequency with equal water-vapor absorption coefficients. Fractional bandwidths, defined as the ratio of the difference between the upper and lower frequencies to the center frequency, are considered at 0.1, 0.2 and 0.3. For an up-looking, ground-based geometry, retrievals of water-vapor absorption are possible only with precipitation present. For a down-looking

aircraft or spacecraft, path-integrated retrievals are possible in both rain and rain-free regions by using the surface as reference target. In the presence of precipitation, equations can be derived as functions of the radar return powers to any range at which backscattered powers are detected. The equations for precipitation and water-vapor attenuation are approximately separable in the sense that for small bandwidths, the equations for rain parameters and water-vapor absorption are weakly coupled.

An error analysis of the approach shows that the biases in the method are relatively small in the rain and snow for percent bandwidths less than about 20% but become significant at bandwidths of 30%. These biases are related to non-Rayleigh scattering effects of the hydrometeors and are determined primarily by phase state and median mass diameter. The bias in the estimate of water vapor density is strongest in the layer of mixed phase hydrometeors associated with the melting layer. The largest source of variability in the estimates arises from signal fluctuations that can easily be as large as the differential signal itself. While the requirement for large numbers of independent samples (to reduce the signal variance) places demands on the radar design and operation, the relatively small frequency separation may allow a 'differential-frequency' implementation where a radar using a single antenna and transceiver can measure the three-frequency returns simultaneously.

Equations for estimates of water vapor absorption and precipitation attenuation are given in section 2, followed by a simulation and error analysis of the water vapor absorption

and density estimates in section 3. Discussions on the algorithm and radar implementation are given in section 4.

2. Equations for precipitation and water-vapor path-attenuation

To simplify the final form of the equations, the following conventions are used. The 'measured' radar reflectivity factor, Z_m, at radar frequency f and range r is defined in terms of the radar return power, P_r, by:

$$Z_m(f,r) = P_r(f,r)r^2 / (C|K_w|^2) \quad (1)$$

where C is the radar constant and $|K_w|^2$ is the dielectric factor of water which, by convention, is taken to be equal to its approximate value (0.93) for frequencies between 3 GHz and 10 GHz and for temperatures between 0 C and 20 C [Battan, 1973]. The unattenuated radar reflectivity factor, or simply radar reflectivity factor, Z, is related to Z_m by:

$$Z(f,r) = Z_m(f,r)\exp\{c\int_0^r [k_p(f,s) + k_c(f,s) + k_v(f,s)]ds\} \quad (2)$$

where k_p, k_c, and k_v are the specific attenuations from precipitation, cloud water, and water vapor respectively, and where the precipitation may include rain, snow and mixed-phase hydrometeors. More generally, contributions from oxygen and cloud ice should be added to (2). If the units of k are taken to be dB km^{-1} then $c=0.2\times\ln 10$; if the units of k are in km^{-1} then c=2. In this paper, we use the former. It is also convenient to define 2-way differential attenuations (dB) to range r for the precipitation and cloud, A_{pc}, and for the water vapor, A_v, by:

$$A_{pc}(f_j, f_i; r) = 2\int_0^r \{[k_p(f_j, s) + k_c(f_j, s)] - [k_p(f_i, s) + k_c(f_i, s)]\} ds \tag{3}$$

$$A_v(f_j, f_i; r) = 2\int_0^r [k_v(f_j, s) - k_v(f_i, s)] ds \tag{4}$$

We define 10 $\log_{10}$ of Z and Z_m by:

$$\begin{aligned} \tilde{Z}_m(f,r) &= 10\log_{10} Z_m(f,r) \\ \tilde{Z}(f,r) &= 10\log_{10} Z(f,r) \end{aligned} \tag{5}$$

Throughout the paper we assume that measurements of P_r, or equivalently Z_m, are made at frequencies (f_l, f_c, f_u) where f_c is taken at the center of the water-vapor absorption line at 22.235 GHz and (f_l, f_u) are chosen such that $f_l < f_c < f_u$ and

$$k_v(f_l) = k_v(f_u) \tag{6}$$

Using the water vapor model described by Ulaby et al. [1981] and Waters [1976], the values of (f_l, f_u) that satisfy (6) are graphed in Fig. 1 as a function of the fractional bandwidth, Δf, which we define by:

$$\Delta f = (f_u - f_l)/f_c \tag{7}$$

If Δf is specified, then (f_l, f_u) can be found from the following approximations:

$$f_l = f_c - 10.936\Delta f + 5.115\Delta f^2 \tag{8}$$

$$f_u = f_c + 11.3\Delta f + 5.114\Delta f^2 \tag{9}$$

As a consequence of the skewed shape of the absorption line, $k_v(f_c+\delta f) > k_v(f_c-\delta f)$ for $\delta f > 0$. For the calculations given later in the paper, percent bandwidths of 10%, 20% and 30% are used where the frequency pairs, in GHz, are given, respectively, by: (f_l, f_u) = (21.248, 23.420), (20.246, 24.694), (19.409, 26.079). It is also worth mentioning that for percent bandwidths of 20% or less a "differential-frequency" implementation of the radar might be feasible. By this term, we mean that a single radar antenna and transceiver would provide measurements of the radar returns at the three frequencies. We will return to this issue later in the paper.

Taking the difference of measured reflectivity factors (in dB) at the upper and lower frequencies, $\tilde{Z}_m(f_u,r) - \tilde{Z}_m(f_l,r)$, and using (6) and the above definitions gives

$$\tilde{Z}_m(f_u,r) - \tilde{Z}_m(f_l,r) = \tilde{Z}(f_u,r) - \tilde{Z}(f_l,r) - A_{pc}(f_u,f_l;r) \tag{10}$$

Similarly, the difference between the measured reflectivity factors (in dB) at the center and lower frequencies, $\tilde{Z}_m(f_c,r) - \tilde{Z}_m(f_l,r)$, can be written:

$$\tilde{Z}_m(f_c,r) - \tilde{Z}_m(f_l,r) = \tilde{Z}(f_c,r) - \tilde{Z}(f_l,r) - (A_{pc}(f_c,f_l;r) + A_v(f_c,f_l;r)) \tag{11}$$

To obtain an estimate of the 2-way differential water vapor absorption, $A_v(f_c, f_l)$, that is approximately independent of the precipitation and cloud attenuation, we assume that

$$A_{pc}(f_c, f_l; r) = \gamma A_{pc}(f_u, f_l; r) \tag{12}$$

Eq. (12) states that the differential attenuation arising from precipitation and cloud between frequencies (f_c, f_l) is equal to some fraction γ of the differential attenuation between frequencies (f_u, f_l). If the precipitation and cloud attenuation is directly proportional to frequency, γ is simply the ratio of frequency differences:

$$\gamma_{Ray} = (f_c - f_l)/(f_u - f_l) \tag{13}$$

and (12) is satisfied exactly. However, because of the frequency dependence of the dielectric constant of water and non-Rayleigh scattering, γ depends on the hydrometeor size distribution so that (12) will generally be incorrect. As will be shown in the results below, the magnitude of the error depends on the nature of the backscattering medium (rain, snow or mixed phase), the parameters of the hydrometeor size distribution, the fractional bandwidth of the radar frequencies that are used, and the choice of γ.

Multiplying (10) by γ and subtracting (11) from the resulting equation yields:

$$\gamma \tilde{Z}_m(f_u, r) + (1-\gamma)\tilde{Z}_m(f_l, r) - \tilde{Z}_m(f_c, r) = E_1 + E_2 + A_v(f_c, f_l; r) \tag{14}$$

where

$$E_1 = \gamma\tilde{Z}(f_u,r) + (1-\gamma)\tilde{Z}(f_l,r) - \tilde{Z}(f_c,r) \tag{15}$$

$$E_2 = A_{pc}(f_c,f_l;r) - \gamma A_{pc}(f_u,f_l;r) \tag{16}$$

The bias term E_2 was discussed above where it was noted that $E_2 = 0$ if (12) holds. The bias term E_1 is a function of the reflectivity factors at the 3 frequencies. Unlike the measured reflectivity factors on the left-hand side of (14), they are not measurable and not easily estimated unless the precipitation retrieval problem is solved in parallel. Similar considerations apply to this term as apply to (12): if the backscattering is Rayleigh, the reflectivity factors are approximately frequency independent and $E_1 \cong 0$.

To estimate $A_v(f_c,f_l)$ from measured data, we assume that the error terms are zero so that

$$\hat{A}_v(f_c,f_l;r) = \gamma\tilde{Z}_m(f_u,r) + (1-\gamma)\tilde{Z}_m(f_l,r) - \tilde{Z}_m(f_c,r) \tag{17}$$

Before presenting an error analysis of (17), we derive equations similar to (10) and (14) by using the backscattered powers from the surface. The equations below are obviously relevant only to a down-looking geometry. On the other hand, unlike (10) and (14), they are applicable in rain-free as well as raining conditions. The measured or apparent radar return power from the surface, P_{sm}, can be written as [Kozu, 1995]:

$$P_{sm}(f,r_s) = [C_s(f)\sigma^0(f)/g(r_s)]\exp\{-0.2\ln 10\int_0^{rs}[k_p(f,s)+k_c(f,s)+k_v(f,s)]ds\} \tag{18}$$

where σ^0 is the normalized radar cross section of the surface (unitless) and C_s is the radar constant for surface scattering which depends on incidence angle, antenna gain, and

frequency. The function $g(r_s)$ represents the range dependence which is equal to r_s^2 for beam-limited (nadir and near-nadir incidence) and r_s^3 for pulse-limited conditions (off-nadir incidence). The radar return power from the surface, P_s, which would be measured in the absence of atmospheric attenuation, can be written:

$$P_s(f,r_s) = C_s(f,r_s)\sigma^0(f)/g(r_s) \tag{19}$$

As before, we define the following quantities:

$$\begin{aligned}
&\tilde{P}_s(f) = 10\log_{10} P_s(f) \\
&\tilde{P}_{sm}(f) = 10\log_{10} P_{sm}(f) \\
&\tilde{\sigma}^0(f) = 10\log_{10} \sigma^0(f)
\end{aligned} \tag{20}$$

Comparing (18)-(20) with (1), (2) and (5) shows that for the case of surface scattering, (10) and (14) become, respectively:

$$\tilde{P}_{sm}(f_u,r_s) - \tilde{P}_{sm}(f_l,r_s) = \tilde{P}_s(f_u,r_s) - \tilde{P}_s(f_l,r_s) - A_{pc}(f_u,f_l;r_s) \tag{21}$$

$$\gamma\tilde{P}_{sm}(f_u,r_s) + (1-\gamma)\tilde{P}_{sm}(f_l,r_s) - \tilde{P}_{sm}(f_c,r_s) = E_{1s} + E_{2s} + A_v(f_c,f_l;r_s) \tag{22}$$

where

$$E_{1s} = \gamma\tilde{P}_s(f_u,r_s) + (1-\gamma)\tilde{P}_s(f_l,r_s) - \tilde{P}_s(f_c,r_s) \tag{23}$$

$$E_{2s} = E_2(r=r_s) = A_{pc}(f_c,f_l;r_s) - \gamma A_{pc}(f_u,f_l;r_s) \tag{24}$$

One difference between the rain and surface scattering equations above is that the E_{1s} error depends on the nature of backscattering not from the hydrometeors, as in E_1, but from the surface. This becomes apparent if (23) is written as:

$$E_{1s} = [\gamma\tilde{\sigma}^0(f_u, r_s) + (1-\gamma)\tilde{\sigma}^0(f_l, r_s) - \tilde{\sigma}^0(f_c, r_s)] + \ldots \quad (25)$$

where the notation '+...' is used to indicate additional terms that are functions of the radar constants. Since these constants are known, or presumed to be known, they can be accounted for in an offset term. A comparison of the bracketed term in (25) with (15) shows that the approximation for the surface scattering is analogous to that used for the precipitation, with the normalized surface cross sections replacing the radar reflectivity factors. If the surface cross section is constant over the frequency span from f_l to f_u the bracketed term in (25) is zero for any γ. Moreover, if γ is set to γ_{Ray}, given by (13), then it can be shown that this term is zero if $\tilde{\sigma}^0$ changes linearly with frequency. Another difference between E_1 and E_{1s} is that an estimate for the latter quantity can be obtained from surface scattering measurements in regions of low path-integrated water vapor. This is analogous to the 'surface-reference technique' where measurements of the surface return in rain-free areas are used to estimate path-attenuation in the presence of rain [Tian et al., 2002; Meneghini et al., 2004]. In particular, an estimate for the differential path-attenuation from cloud and hydrometeors follows directly from (21) where the term $\tilde{P}_s(f_u, r_s) - \tilde{P}_s(f_l, r_s)$ is approximated by surface returns measured in clear conditions. Since the main subject of the paper is the feasibility of height-profiled water vapor

estimates in rain, we focus the error analysis on the range-dependent estimate of differential water vapor attenuation given by (17).

3. Error analysis of water-vapor profiling retrievals

3a. Description of the simulation

To analyze errors in the estimate of differential water vapor given by (17) we construct a simple stratiform storm model derived from disdrometer-measured raindrop size distributions [Meneghini et al., 2003]. For each size distribution we compute the median mass diameter, D_0 (mm) and number concentration, N_t (m^{-3}). To complete the specification, we assume that the drop diameter distribution, N(D) (mm^{-1} m^{-3}), follows a gamma distribution with a fixed shape parameter, μ, equal to 2 [Ulbrich, 1983]:

$$N(D) = N_0 D^{\mu} \exp[-(3.67+\mu)D/D_0] \tag{26}$$

where

$$N_0 = N_t (3.67+\mu)^{\mu+1} / (D_0^{\mu+1} \Gamma(\mu+1)) \tag{27}$$

and where Γ is the gamma function given by:

$$\Gamma(x) = \int_0^{\infty} t^{x-1} e^{-t} dt \tag{28}$$

The storm structure is assumed to be composed of a layer of snow, from 4 to 5 km above the surface, a transition region of mixed-phase hydrometeors, from about 3.5 to 4 km and a rain layer from about 3.5 km to the surface. The fractional melt water in the melting layer is prescribed as a function of the initial snow size, mass density and distance below the 0^0 isotherm [Yokoyama and Tanaka, 1984]. The effective dielectric constant of the

mixed phase particles is given by the effective medium approximation [Bohren and Battan, 1980]. For the results shown here, the snow mass density is fixed and equal to 0.2 g cm^{-3}. The location and density of the cloud water are also included although this contribution is not critical to the behavior of the water vapor retrievals. The temperature lapse rate is taken to be constant and equal to 6 C/km so that with the 0^0 isotherm at 4 km, the surface temperature is 24 C. To focus on the bias and random errors of the estimate in this set of examples, the relative humidity is taken to be constant from the surface to a height of 5 km and equal to 80%. From this simple storm model, approximately 400 range profiles of Z_m at the three frequencies can be generated, where each profile is derived from measured raindrop size distribution parameters and consists of the returns from the snow, mixed phase and liquid hydrometeors, and includes effects of absorption from cloud water, water vapor and molecular oxygen. Note also that the range resolution is taken to be 125 m so that the profile consists of 40 gates or bins. The simulated radar measurements at $f = f_l, f_c, f_u$ are computed from the following set of equations:

$$Z_m(f,r) = c_Z[\int_0^\infty \sigma_b(f,D)N(D,s)dD]\exp[-0.2\ln 10 \int_0^r (k_p(f,s)+k_c(f,s)+k_v(f,s))ds] \qquad (29)$$

where the specific attenuations (dB km^{-1}) are given by:

$$k_p(f) = 4.343\times10^{-3}\int_0^\infty \sigma_e(f,D)N(D,s)dD \qquad (31)$$

$$k_c(f) = [(4.343\times10^{-2}\times 6\pi f)/c_0]\,\mathrm{Im}(-K_w)M_c \qquad (32)$$

$$k_v(f) = 2f^2\rho_v(300/T)^{3/2}\gamma_1\{(300/T)e^{-644/T}/[(494.4-f^2)^2+4f^2\gamma_1^2]+1.2\times10^{-6}\} \qquad (33)$$

with

$$c_Z = c_0^4 / (f^4 \pi^5 \, |K_w|^2) \tag{34}$$

$$K_w = \frac{m^2 - 1}{m^2 + 2} \tag{35}$$

$$\gamma_1 = 2.85(P/1013)(300/T)^{0.626}[1 + 0.018\rho_v T/P] \tag{36}$$

where P is the pressure (millibar), T is temperature (K), ρ_v is the water vapor density (g m^{-3}), c_0 is the speed of light (mm s^{-1}), m is the complex index of refraction of the (cloud) water, M_c is the cloud water content (g m^{-3}), and $\sigma_b(f, D)$, $\sigma_e(f, D)$ are, respectively, the backscattering and extinction cross sections (mm^2) of a sphere of diameter D at frequency f. The expression for k_v above is taken from results of Waters (1976) and Ulaby et al. (1981) for f < 100 GHz. It is important to note that in (33) the frequency is to be specified in GHz; in all other equations the frequency is to be expressed in Hz. Following Ulaby et al. (1981), the contribution from molecular oxygen is also included.

The error analysis consists of computing the right-hand side of (17) using (29) – (36) and comparing the estimated 2-way differential vapor absorption profile with the assumed profile as calculated from (4), (33) and (36). To compute the right-hand side of (17), a value of γ is required. Although the approximation from (13) can be used, it was found by trial and error that somewhat smaller values reduce the bias. For the results shown in the paper, we use γ=0.44 (10% bandwidth), γ=0.42 (20%), and γ=0.39 (30%) instead of the results from (13) which give: γ_{Ray}=0.455 (10% bandwidth), γ_{Ray}=0.447 (20%), and γ_{Ray} =0.424 (30%). An exception to these assumptions is the case presented in Fig. 2, explained below, where we have chosen γ=0.39 for the 20% bandwidth case to emphasize

the bias in the estimate; i.e., the bias is qualitatively the same but smaller when the value γ=0.42 is used.

Apart from the bias errors, E_1 and E_2, described in the previous section, an important additional source of error arises from the finite number of independent samples used to estimate the radar return power and Z_m. For a square-law detector, where the output of each sample is proportional to the return power, the deterministic quantity $\tilde{Z}_m$ is replaced by $(\tilde{Z}_m + g)$, where, for the number of samples, n, greater than about 10, the random variable g can be approximated by a zero mean Gaussian with variance [Bringi et al., 1983]:

$$\mathrm{var}(g) = 4.343^2\{\pi^2/6 - \sum_{m=1}^{n-1} m^{-2}\} \tag{37}$$

For figures 2 through 8, n is taken to be a large number (64,000) so that the bias terms can be examined without large background variability from finite sampling.

3b. Error estimate of differential water vapor attenuation

The top panel of Fig. 2 shows simulations of $\tilde{Z}_m(f_c)$ over approximately 400 'observations' (x-axis) over the 5 km storm height (y-axis). The results clearly show a bright-band, corresponding to returns from the partially melted snow, in the ranges just below the 0^0 isotherm at 4 km. Since the radar is assumed to be above the storm viewing along nadir, effects of attenuation are evident by the reduction in the measured reflectivity factor as the penetration depth increases. Results for the measured differential reflectivity for the upper and lower frequencies, $\tilde{Z}_m(f_u) - \tilde{Z}_m(f_l)$, are shown

in the second panel from the top. A 20% bandwidth has been chosen so that $f_u = 24.694GHz$ and $f_l = 20.246GHz$. The magnitude of $\tilde{Z}_m(f_u) - \tilde{Z}_m(f_l)$ depends on the drop size distribution, phase of the hydrometeors (solid, liquid or partially melted), and the cumulative attenuation by precipitation and cloud. However, it is independent of water vapor since $k_v(f_u) = k_v(f_l)$.

The bottom two panels of Fig. 2 show the estimated and assumed values of the 2-way differential water vapor absorption, $A_v(f_c, f_l; r)$, where the estimated value is computed from the right-hand side of (17). Despite the large number of independent samples (64,000), variations caused by the finite number of samples are still evident. Superimposed on the fluctuations are biases that are seen to be well correlated with decreases in the $\tilde{Z}_m(f_u) - \tilde{Z}_m(f_l)$ field shown in the panel above; as already noted, the bias terms have been exaggerated by choosing γ=0.39 for this plot.

To understand how the bias in $A_v(f_c, f_l; r)$ depends on the parameters of the precipitation, it is useful to examine some of the relevant quantities as functions of the median mass diameter, D_0. The results in Figs. 3 and 4 are taken from the lowest gate, just above the surface so that the attenuations are approximately the same as the total path attenuations. Shown in the top panel of Fig. 3 are values of $\tilde{Z}_m(f_u) - \tilde{Z}_m(f_l)$ versus D_0. Variations in this quantity originate from two sources: non-Rayleigh scattering and attenuation effects from the precipitation and cloud. The non-Rayleigh source of variability can be seen in the results for $\tilde{Z}(f_u) - \tilde{Z}(f_l)$ shown in the middle panel of Fig. 3. Since the 'shape' parameter, μ, of the size distribution has been fixed, $\tilde{Z}(f_u) - \tilde{Z}(f_l)$ is a function only of D_0

and independent of the number concentration. A scatter plot of the differential path attenuation from cloud and precipitation, $A_{pc}(f_u, f_l; r)$, is shown in the bottom panel. Note that this quantity depends on N_t as well as D_0 as seen by the variability in this quantity for fixed D_0. Since the cloud liquid water was taken to be zero for this simulation, the attenuation arises entirely from the hydrometeors. The addition of an integrated cloud water content of 1 kg/m^2 for all cases yields an increase in $A_{pc}(f_u, f_l; r)$ of about 0.4 dB (not shown) but has a negligible effect on the bias errors shown in the lower two panels of Fig. 4.

The top panel of Fig. 4 shows the estimated (X data points) and true values (solid line) of the differential water vapor absorption, $A_v(f_c, f_l; r)$. The variability in the estimates for constant D_0 is the result of finite sampling and reduces to zero as n goes to infinity. In addition to the variability is a bias which is negative for D_0 values up to about 2 mm and slightly positive above 2 mm. This bias is the sum of E_1 and E_2 displayed in the bottom two panels of Fig. 4. The behavior of E_1 is determined almost exclusively by the median mass diameter; on the other hand, variability at a fixed D_0, indicating dependence on number concentration, can be seen in the E_2 term for large D_0 values. The results imply that if the rain estimation problem can be solved in parallel (or iteratively) with the water absorption estimate, the D_0 (and N_t) values, as estimated from the precipitation algorithms can, in principle, be used to correct for biases in the water vapor retrieval. Although a quantitative description of algorithms of this type is beyond the scope of the paper, a qualitative description of a possible approach is outlined in section 4.

The results in Figs. 3 and 4 are taken from the range gate in rain at the bottom of the column. For the case shown in Figs. 5 and 6, the range is taken to be just above the melting layer at a snow depth of about 0.9 km. Comparison of the results of Fig. 5 and Fig. 3 show a number of obvious differences between the two cases. The differential reflectivity factor in snow, $\tilde{Z}(f_u)-\tilde{Z}(f_l)$, shown in the middle panel of Fig. 5, is a monotonically decreasing function of D_0 (the median mass diameter of the melted snow); moreover, as the attenuation through snow is small (bottom panel), the behavior of the measured differential reflectivity factor, $\tilde{Z}_m(f_u)-\tilde{Z}_m(f_l)$, shown in the top panel, is primarily determined by $\tilde{Z}(f_u)-\tilde{Z}(f_l)$.

The estimated and true values of the water vapor absorption to this range are shown in the top panel of Fig. 6. Notice that the magnitude of the fluctuations is essentially the same as before but because the water vapor absorption to this range is small, the relative error caused by the finite sampling is much higher. On the other hand, the biases in the estimate are small. This can be seen in the bottom panels where E_2 is approximately zero while E_1 is small up to moderate D_0 values and positive for large D_0.

In the melting layer, the E_2 bias term remains relatively small; however, the E_1 bias term is significant and changes from gate to gate. Plots of E_1 versus D_0 are shown in Fig. 7 for four range gates within the melting layer. For gates 13 and 15, the sign of the bias is negative for small D_0 and positive for larger values. As will be shown later, this bias has a strong effect on the water vapor retrievals in and about the melting layer.

Before looking at statistics of the $A_v(f_c, f_l; r)$ estimates, it is instructive to view individual retrievals. In Fig. 8, five arbitrarily chosen profiles of $A_v(f_c, f_l; r)$, from the results of Fig. 1, are represented by the thin solid lines. The true (assumed) profile is represented by the heavy solid line. The results for the nearly 400 profiles are indicated by the + signs; that is, at each range gate, approximately 400 data points are displayed corresponding to the estimated values of $A_v(f_c, f_l; r)$ at range r. The behavior of the individual profiles indicate that even for a very large number of independent samples, the fluctuations in $A_v(f_c, f_l; r)$ with range can be substantial. Computing the differential specific absorption without smoothing in range or further averaging in space or time would clearly lead to large errors.

The results shown in Fig. 8 are from the single simulation shown in Fig. 1. To obtain accurate estimates of the mean and standard deviation as a function of range, 200 simulations of the retrievals were made. Note that from realization to realization, the set of drop size distributions is fixed and only the $\widetilde{Z}_m$ are changed to simulate the effects of finite sampling. The results are shown in Figs. 9-11 for bandwidths of 20%, 30% and 10%, respectively. Unlike the previous results, a more realistic number of independent samples (n=4000) is used. For each figure, images of the estimated and true values of the differential absorption, $A_v(f_c, f_l; r)$, for a single simulation are shown in the top panels; in the bottom panel are shown the true value (solid line) along with the mean (X) and twice the standard deviation of the estimate (vertical height of error bar) as a function of range. As in Fig. 8, gate 40 represents the range gate just above the surface.

The three sets of results show that the standard deviation is independent of range so that the relative error decreases with distance from the radar since the path absorption increases. In snow, the bias in $A_v(f_c, f_l; r)$ is small. In the rain, however, the bias for the 30% case (Fig. 10) is relatively large. The bias decreases in going to smaller bandwidths so that the 10% case (Fig. 11) shows the smallest bias. On the other hand, the fractional standard deviation (standard deviation divided by the mean) is largest for the 10% case and decreases in going to 20% and again to 30% bandwidth.

3c. Error estimates of water vapor retrievals

A range derivative of the differential path attenuation, $A_v(f_c, f_l)$, yields the differential specific water vapor absorption, $k_v(f_c) - k_v(f_l)$. To reduce the variability in $A_v(f_c, f_l)$, a 5-gate moving average is done, followed by a differencing over successive 5-gate intervals. After normalizing by the range difference, this procedure gives $k_v(f_c, r_j) - k_v(f_l, r_j); j = 3,...,38$ where estimates at the two lower-most and upper-most range gates are discarded. From the estimate of differential specific absorption and model temperature (with lapse rate as before of 6 C km^{-1}) and pressure profiles, the water vapor density and relative humidity are computed. The 'true' temperature and pressure profiles are assumed to be Gaussian random variables with a mean given by the model profiles with standard deviations of 1 K and 2 millibar, respectively, as derived from the results of 200 soundings in the South China Sea. Note that the 'true' ρ_v field is computed from the assumed RH and randomly varying temperature and pressure profiles. The simulated storm parameters are similar to those used previously with the exceptions that the integrated cloud water content is taken to be 1 kg/m^2 and the relative humidity is

assumed to be 100% above the 0^0 isotherm, decreasing linearly to 70% at the surface. Results are shown only for 20% bandwidth case with the number of samples, n, equal to 16,000 samples. For n=64,000 the RMS errors in the water vapor and RH retrievals in the lowest 3 km are approximately halved while for n=4,000 the errors are approximately doubled.

Shown in the top left panel of Fig. 13 are the estimated (dashed line) and assumed (solid line) mean values of $A_v(f_c, f_l)$ computed over the set of about 400 profiles. On the top right panel are the estimated (dashed line) and assumed mean values of $k_v(f_c) - k_v(f_l)$ using the averaging procedures described above. Biases in $A_v(f_c, f_l)$ can be seen to increase just below the melting layer at 4 km and assume nearly a constant value from about 3 km down to the surface. Examination of the $k_v(f_c) - k_v(f_l)$ estimate reveals a large negative bias associated with scattering in the melting layer. This is directly related to the E_1 bias term shown in Fig. 7. However, because of the need to smooth the data, the influence of this error extends into the snow above and the rain below. Standard deviations of $A_v(f_c, f_l)$ and $k_v(f_c) - k_v(f_l)$ are shown in the bottom panels. Since the assumed pressure and temperature profiles were randomized, the 'true' values of $A_v(f_c, f_l)$ and $k_v(f_c) - k_v(f_l)$ are also random with standard deviations given by the solid lines. The standard deviations of the estimated profiles of $A_v(f_c, f_l)$ and $k_v(f_c) - k_v(f_l)$ are given by the dashed lines in the lower panels; the greater variability in estimated profiles is caused by the finite number of samples. As noted above, increasing n by a factor of 4 reduces the estimated standard deviations by about a factor of 2.

Corresponding statistics for the water vapor density, ρ_v, and RH are shown in Fig. 14 where it can be seen that negative biases in $k_v(f_c) - k_v(f_l)$ at and about the melting layer produce large negative biases in ρ_v and RH over the same range. Although the vertical extent of the bias can be narrowed with an averaging interval less than five, this leads to higher standard deviations in the estimates. As in the previous plot, the standard deviations of the true and estimated fields are shown in the lower panels.

The RMS errors for ρ_v and RH are presented in the top panels of Fig. 15 and the normalized errors are shown in the bottom panels, i.e., the RMS error divided by the true value. For ρ_v, the relative errors in the bottom 3 km are between 20% and 28%; above 3 km, the errors become as large as 32%. Similar accuracies can be seen in RH, with relative errors between 20% and 28% below 3 km and larger errors above 3 km. If the assumed temperature and pressure are taken equal to the model values, the relative errors decrease by about 4%. Increasing the sample number to 64,000 decreases the relative errors in ρ_v and RH to between 12% to 16% in the lowest 3km. In the melting layer, however, the maximum relative error is about 25%. Increasing the bandwidth to 30% decreases the standard deviations in $k_v(f_c) - k_v(f_l)$, ρ_v, and RH in the lowest 3 km but also produces higher negative biases and relative errors in and about the melting layer. For the case of n=16,000 and 30% bandwidth, the standard deviations in ρ_v and RH decrease to about 16% in the lowest 3 km but exhibit a maximum relative error of about 36% in the melting layer.

More sophisticated averaging and smoothing techniques might serve to reduce the RMS errors. As already pointed out, information on the median mass diameter of the

hydrometeors, particularly in the melting layer, would serve to reduce the bias. Further investigations, and, ultimately, an analysis of measured data, will be needed to address these issues.

4. Discussion and Summary

The approach used here has some similarities to the differential absorption lidar (DIAL) technique in that it uses frequencies on and off line center to estimate the strength of absorption. The fact that precipitation is the background scattering medium, however, implies that the differential attenuation by hydrometeors can easily be as large as water vapor absorption; moreover, non-Rayleigh backscattering effects at these frequencies can be comparable in magnitude to attenuation and absorption. By the use of 3-frequencies, we can take advantage of the fact that differential attenuation from precipitation and cloud is approximately an odd function with respect to the center frequency while the differential water vapor absorption is approximately an even function.

In deriving an expression for the differential vapor absorption, the critical assumption is that the differential attenuation from cloud and precipitation between the upper and lower frequencies can be expressed as a fraction of the differential attenuation between the center and lower frequencies. Results of the simulations show that this assumption leads to biases in the estimate of water vapor density that become larger as the bandwidth increases. While the biases are small in snow, they are particularly strong in the melting layer and lead to large negative biases in the vapor density estimates in and around the melting layer.

Although the focus of the paper is estimation of water vapor, the approach also offers the potential of precipitation estimation. Because of the choice of lower and upper frequencies, the differential measured reflectivity factor, $\tilde{Z}_m(f_u) - \tilde{Z}_m(f_l)$, is function only of the characteristics of the precipitation and cloud and is independent of water vapor. If the differential path attenuation from cloud and precipitation can be estimated then $\tilde{Z}(f_u) - \tilde{Z}(f_l)$ follows directly from (10). But it is clear from the results of Fig. 3 and Fig. 5 that from $\tilde{Z}(f_u) - \tilde{Z}(f_l)$ an estimate of the D_0 can be obtained. Moreover, an estimate of the number concentration N_t can be obtained from the radar equation, (1). To start the procedure requires an initial or estimated path attenuation. One such estimate can be obtained from (21) by measuring the surface return powers in clear regions. However, as recently shown by Mardiana et al. (2004), the equations also can be solved iteratively without an independent path-attenuation estimate. In either case, the procedure yields estimates of the size distribution parameters along the profile. The D_0 and N_t values can be used, in turn, to improve the estimate of the differential water vapor absorption by using the information to estimate the bias terms E_1 and E_2. A drawback to the procedure is that the equation for N_t, as derived from the radar equation, is a function $k_v(f_l)$ or $k_v(f_u)$. Although the term is usually small for the 20% and 30% bandwidth cases relative to the hydrometeor attenuation, it represents an additional error source in the precipitation retrieval problem. In principle, just as the hydrometeor size distribution parameters can be used to correct for biases in the water vapor retrieval, the water vapor retrieval can be used to account for this contribution in the precipitation retrieval. Whether iterating between solutions to the precipitation and water vapor equations will provide stable solutions is not clear, however.

Another way to view the approach is as a variation of the differential-frequency implementation. In this approach, a single antenna and transceiver are used to transmit and receive signals at more than one frequency. However, this requires a wide-band power amplifier and a wide-band antenna. Wide-band power amplifiers with bandwidths up to 20% are now available in some frequency bands [J. Carswell, personal communication]. For broad-band solid state amplifiers, with high duty cycles but low peak powers, pulse-compression techniques can be used to achieve fine range resolution. Averaging the data to a coarser vertical resolution may provide a sufficient number of independent samples to make the measurement technique feasible without excessive space or time averaging. Two other methods of increasing the effective number of independent samples are frequency agility and data "whitening" [Koivunen and Kostinski, 1999; Torres and Zrnic, 2003; Torres et al., 2004]. Another requirement of the radar would be well-matched beamwidths at the three frequencies. Since the total differential path absorption for a 20% bandwidth is on the order of 1 dB, any mismatches in the radar resolution volumes will have a strong effect on accuracy particularly in convective rain where vertical and horizontal gradients in the reflectivity field can be large. Horn-lens and parabolic antennas are inherently broad-band and should be capable of good performance over a 20% bandwidth. Nevertheless, detailed calculations would be needed to assess the degree of beam matching needed relative to the gradients in the reflectivity field.

Acknowledgements: We wish to thank Professor Ramesh C. Srivastava for suggesting the use of multiple frequencies for the measurement of water vapor.

REFERENCES

Alber, C., R.H. Ware, C. Rocken, and F.S. Solheim, 1997: GPS surveying with 1 mm precision using corrections for atmospheric slant path delay. *Geophys. Res. Lett.*, **24**, 1859-1862.

Battan, 1973: ***Radar Observation of the Atmosphere***. The University of Chicago Press, 324 pp.

Behrendt, A., T. Nakamura, M. Onishi, R. Baumgart, T. Tsuda, 2002: Combined Raman lidar for the measurement of atmospheric temperature, water vapor, particle extinction coefficient and particle backscatter coefficient. *Appl. Opt.*, **41**, 7657.

Bevis, M., S. Businger, T.A. Herring, C. Rocken, R.A. Anthes, and R.H. Ware, 1992: GPS meteorology: Remote sensing of atmospheric water vapor using the Global Positioning System. *J. Geophys. Res.*, **97**, 15,787-15,801.

Bohren, C.F. and L.J. Battan, 1980: Radar backscattering by inhomogeneous precipitation particles. *J. Atmos. Sci.*, **37**, 1821-1827.

Brassington, D.J., 1982: Differential absorption lidar measurements of atmospheric water vapor using an optical parametric oscillator source. *Appl. Opt.*, **21**, 4411-4416.

Bringi, V.N., T.A. Seliga, and S.M. Cherry, 1983: Statistical properties of the dual-polarization differential reflectivity (ZDR) radar signal. *IEEE Trans. Geosci. Remote Sens.*, **GE-21**, 215-220.

Hagen, D.E., et al., 2004: Validating AIRS upper atmosphere water vapor retrievals using aircraft and balloon in situ measurements. *Geophys. Res. Lett.*, **31**, L21103, doi:10.1029/2004GL020302.

Koivunen, A.C. and A.B. Kostinski, 1999: The feasibility of data whitening to improve performance of weather radar. *J. Appl. Meteor.*, **38**, 741-749.

Kozu, T., 1995: A generalized surface echo radar equation for down-looking pencil beam radar. *IEICE Trans. Commun.*, **E78-B**, 1245-1248.

Liljegren, J.C., 2004: Improved retrievals of temperature and water vapor profiles with a twelve-channel radiometer. Eighth Symp. On Integrated Observing and Assimilation Systems for Atmosphere, Oceans and Land Surface. Amer. Meteor. Soc., 11-15 Jan., Seattle, WA.

Mardiana, R., T. Iguchi, and N. Takahashi 2004: A dual-frequency rain profiling method without the use of surface reference technique. *IEEE Trans. Geosci. Remote Sens.*, **42**, 2214-2225.

Meneghini, R., J.A. Jones, T. Iguchi, K. Okamoto, and J. Kwiatkowski, 2004: A hybrid surface reference technique and its application to the TRMM precipitation radar. *J. Atmos. Ocean. Technol.*, **21**, 1645– 1658.

Meneghini, R., S.W. Bidwell, R. Rincon, and G.M Heymsfield, 2003: Differential-frequency Doppler weather radar: theory and experiment. *Radio Sci.*, **38**, 8040, doi:10.1029/2002RS002656.

Rosenkranz, P.W., 2001: Retrieval of temperature and moisture profiles from AMSU-A and AMSU-B measurements. *IEEE Trans. Geosci. Remote Sens.*, **39**, 2429-2435.

Schlüssel, P., and P. Bauer, 1993: Rainfall, total water, ice water and water vapor over sea from polarized microwave simulations and Special Sensor Microwave/Imager data. *J. Geophys. Res.*, **98**, 20737-20759.

Schmetz, J. and O.M. Turpeinen, 1998: Estimation of the upper tropospheric relative humidity field from Meteosat water vapour image data. *J. Appl. Meteor.*, **27**, 889-899.

Schultz, J., P. Schlüssel, and H. Grassl, 1993: Water vapour in the atmospheric boundary layer over oceans from SSM/I measurements. *Int. J. Remote Sens.*, **14**, 2773-2789.

Solheim, F., J.R. Godwin, E.R. Westwater, Y. Han, S.J. Keihm, K. Marsh, and R. Ware, 1998: Radiometric profiling of temperature, water vapor and cloud liquid water using various inversion methods. *Radio Sci.*, **33**, 393-404.

Tian, L., G.M. Heymsfield, and R.C. Srivastava, 2002: Measurement of attenuation with airborne and ground-based radar in convective storms over land and its microphysical implications. *J. Appl. Meteor.*, **41**, 716-733.

Tian, L., R.C. Srivastava, G.M. Heymsfield, and L. Li, 2004: Estimation of raindrop-size distribution in stratiform rain from dual-wavelength airborne Doppler radars. Proc. Second TRMM International Science Conference, September 5-10, 2004, Nara, Japan.

Torres, S.M., C.D. Curtis, J.R. Cruz, 2004: Pseudowhitening of weather radar signals to improve spectral moment and polarimetric variable estimates at low signal-to-noise ratios. *IEEE Trans.Geosc.i and Remote Sens,* **42**, 941-949.

Torres, S.M., D. S. Zrnic, 2003: Whitening in range to improve weather radar spectral moment estimates. Part I: formulation and simulation. *J. Atmos. Oceanic Technol.*, **20,** 1433-1448.

Ulaby, F. T., R.K. Moore, and A.K. Fung, 1981: ***Microwave Remote Sensing.*** Vol. 1., Addison-Wesley, 456pp.

Ulbrich, C.W. 1983: Natural variations in the analytical form of the raindrop size distribution. *J. Climate Appl. Meteor.*, **22**, 1764-1775.

Wang, J.R., S. H. Melfi, P. Racette, D. N. Whiteman, L. A. Chang, R. A. Ferrare, K. D. Evans, F. J. Schmidlin, 1995: Simultaneous Measurements of Atmospheric Water Vapor with MIR, Raman Lidar, and Rawinsondes. *J. Appl. Meteor.*, **34**, 1595-1607.

Waters, J.W., 1976: Absorption and emission of microwave radiation by atmospheric gases, in *Methods of Experimental Physics*, M.L. Meeks, ed., 12, Part B, Radio Astronomy, Academic Press, Section 2.3.

Westwater, E.R., Y. Han, M.D. Shupe, and S.Y. Matrosov, 2001: Analysis of integrated cloud liquid and precipitable water vapor retrievals from microwave radiometers during the surface heat budget of the Arctic Ocean project. *J. Geophys. Res.*, **106**, D23, 32,019-32,030.

Whiteman, D.N., 2003: Examination of the traditional Raman lidar technique. II. Evaluating the ratios for water vapor and aerosols. *Appl. Opt.*, **42**, 2593-2608.

Wilheit, T. T., 1990: An algorithm for retrieving water vapor profiles in clear and cloudy atmospheres from 183 GHz radiometric measurements, Simulation studies. *J. Appl. Meteor.*, **29**, 508-515.

Yokoyama, T. and H. Tanaka, 1984: Microphysical processes of melting snowflakes detected by two-wavelength radar, *J. Meteor. Soc. Japan*, **62**, 650-666.

Figure Captions:

Fig. 1: Top: Specific absorption of water vapor (dB/km) for water vapor densities (g/m^3) of 8.75 (lowest), 13.15, 17.5 (highest) and the frequencies at which the absorption is equal for bandwidths of 10%, 20% and 30%. Bottom: Upper and lower frequencies giving equal water vapor absorptions versus percent bandwidth. Solid lines represent numerical values; dashed lines represent quadratic approximations given by (8) and (9).

Fig. 2: Simulated fields of measured reflectivity factor at f_c=22.235 GHz (top), differential measured reflectivity factor (second from top), estimated differential water vapor absorption (third from top) and assumed differential water vapor absorption (bottom). All units are in dB. (γ=0.39).

Fig. 3: Measured (top) and actual (center) differential reflectivity factor and differential path attenuation from precipitation (bottom) for a range gate near the surface versus the median drop diameter, D_0. All units are in dB.

Fig. 4: Top: Assumed (solid line) and estimated differential water vapor absorption (X) versus median raindrop diameter for a range gate near the surface; Center: Bias term E_1; Bottom: Bias term E_2. γ=0.42.

Fig. 5: Measured (top) and 'actual' (center) differential reflectivity factor and differential path attenuation (bottom) for a range gate in the snow just above the melting layer versus median drop diameter of melted particles, D_0.

Fig. 6: Top: Assumed (solid line) and estimated differential water vapor absorption (X) in snow versus median drop diameter of melted particles; Center: Bias term E_1; Bottom: Bias term E_2. γ=0.42.

Fig. 7: Bias term E_1 for four range gates within the melting layer (11, 13, 15, 17) versus median mass diameter of the equivolume raindrops.

Fig. 8: Five profiles of estimated differential water vapor absorption (thin lines) and assumed differential absorption (thick line) versus range gate number (125 m) from storm top. Results from all estimated profiles are indicated by the '+" symbol. γ=0.42.

Fig. 9: Estimated (top) and assumed (center) differential water vapor absorption; bottom: assumed (solid line) and the mean (X) and twice the standard deviation (vertical bars) of the estimates versus range gate number. A bandwidth of 20% is assumed with γ=0.42.

Fig. 10: Same as Fig. 9 but for a bandwidth of 30%. γ=0.39.

Fig. 11: Same as Fig. 10 but for a bandwidth of 10%. γ=0.44.

Fig. 12. Top left: Mean profiles of estimated (dashed line) and assumed (solid) differential water vapor attenuation versus height. Top right: Mean profiles of estimated (dashed line) and assumed (solid) differential specific attenuation. Bottom left: Standard deviation of estimated (dashed line) and assumed (solid) differential water vapor attenuation. Bottom right: Standard deviation of estimated (dashed line) and assumed specific differential attenuation. n=16,000 and 20% bandwidth.

Fig. 13. Top left: Mean profiles of estimated (dashed line) and assumed (solid) water vapor density versus height. Top right: Mean profiles of estimated (dashed line) and assumed (solid) relative humidity, RH. Bottom left: Standard deviation of estimated (dashed line) and assumed (solid) water vapor density. Bottom right: Standard deviation of estimated (dashed line) relative humidity. n=16,000 and 20% bandwidth.

Fig. 14. Top left: RMS error in estimate of water vapor density versus height. Top right: RMS error in estimate of relative humidity. Bottom left: Relative error in water vapor density estimate (RMS normalized by true value). Bottom right: Relative error in relative humidity estimate. n=16,000 and 20% bandwidth.

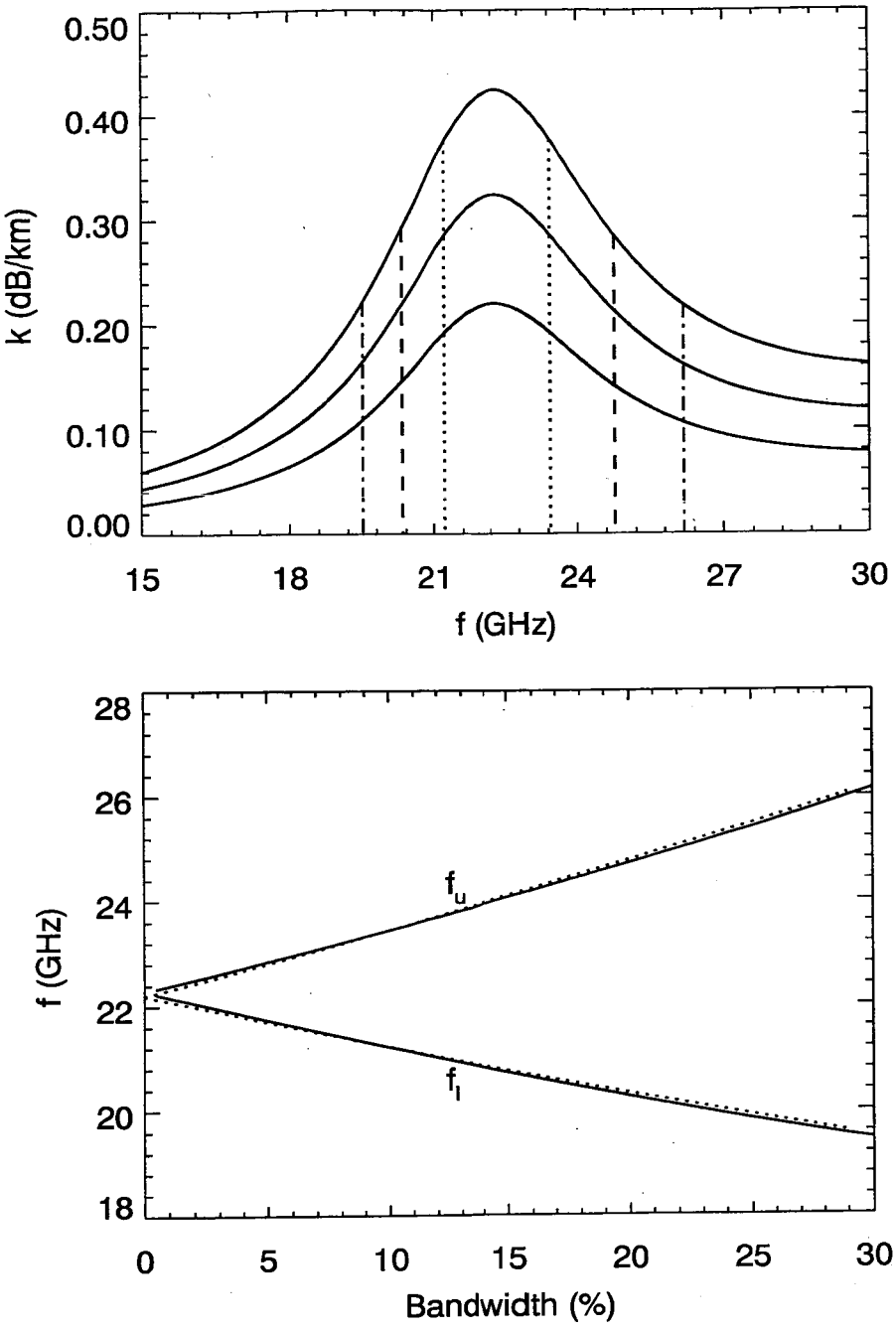

Fig.1. Top: Specific absorption of water vapor (dB/km) for water vapor densities (g/m^3) of 8.75 (lowest), 13.15, 17.5 (highest) and the frequencies at which the absorption is equal for bandwidths of 10%, 20% and 30%. Bottom: Upper and lower frequencies giving equal water vapor absorptions versus percent bandwidth. Solid lines represent numerical values; dashed lines represent quadratic approximations given by (8) and (9).

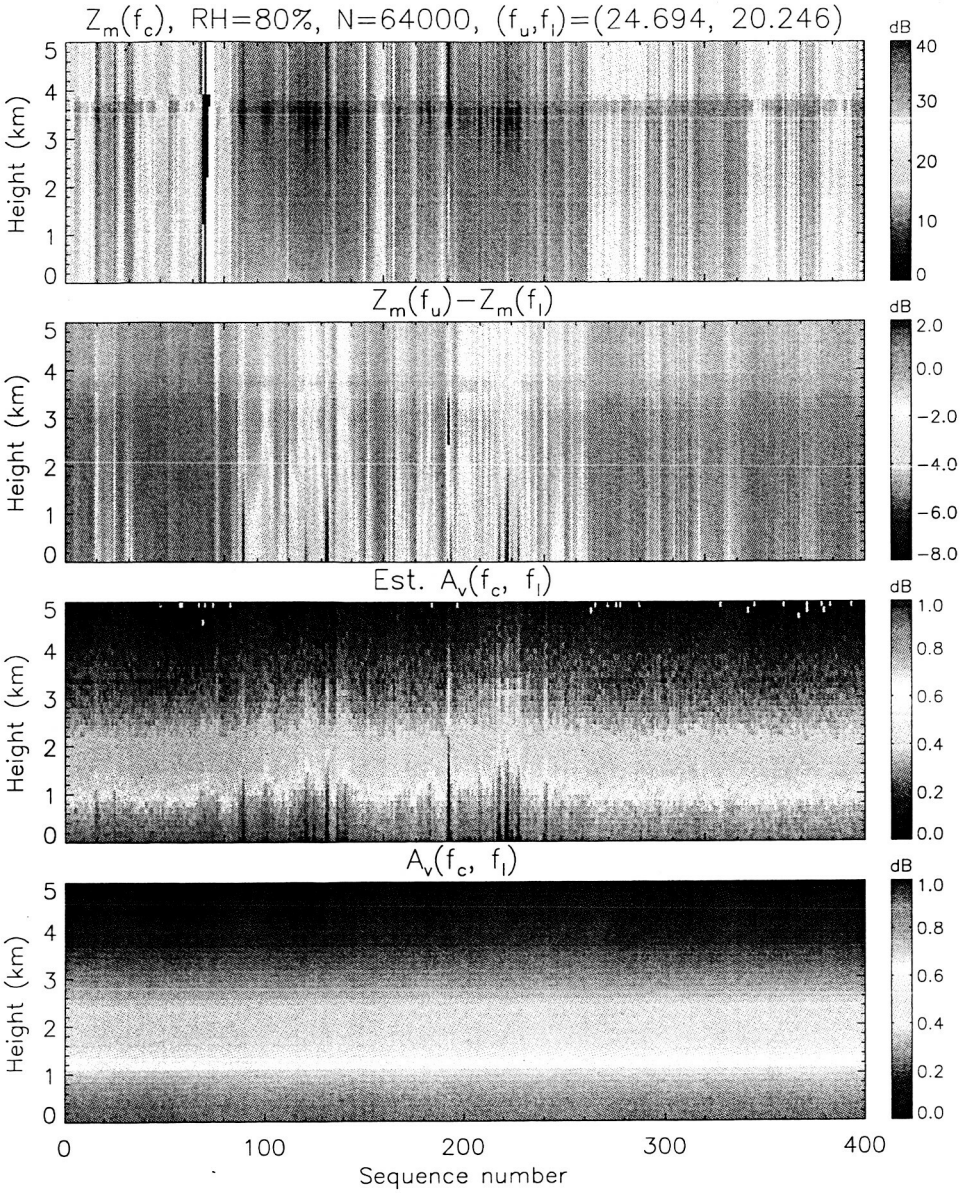

Fig. 2. Simulated fields of measured reflectivity factor at f_c=22.235 GHz (top), differential measured reflectivity factor (second from top), estimated differential water vapor absorption (third from top) and assumed differential water vapor absorption (bottom). All units are in dB. (γ=0.39).

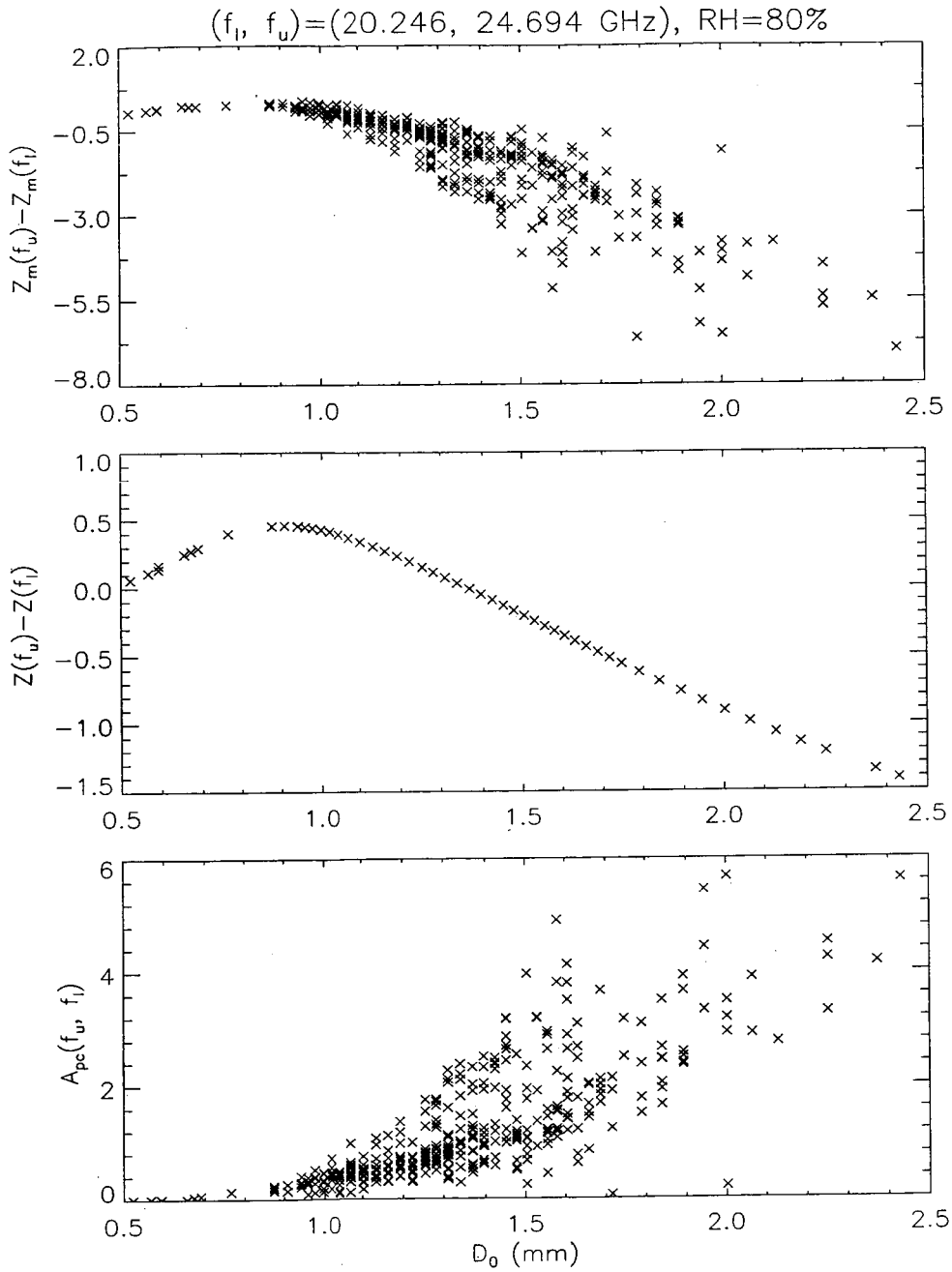

Fig.3. Measured (top) and actual (center) differential reflectivity factor and differential path attenuation from precipitation (bottom) for a range gate near the surface versus the median drop diameter, D_0. All units are in dB.

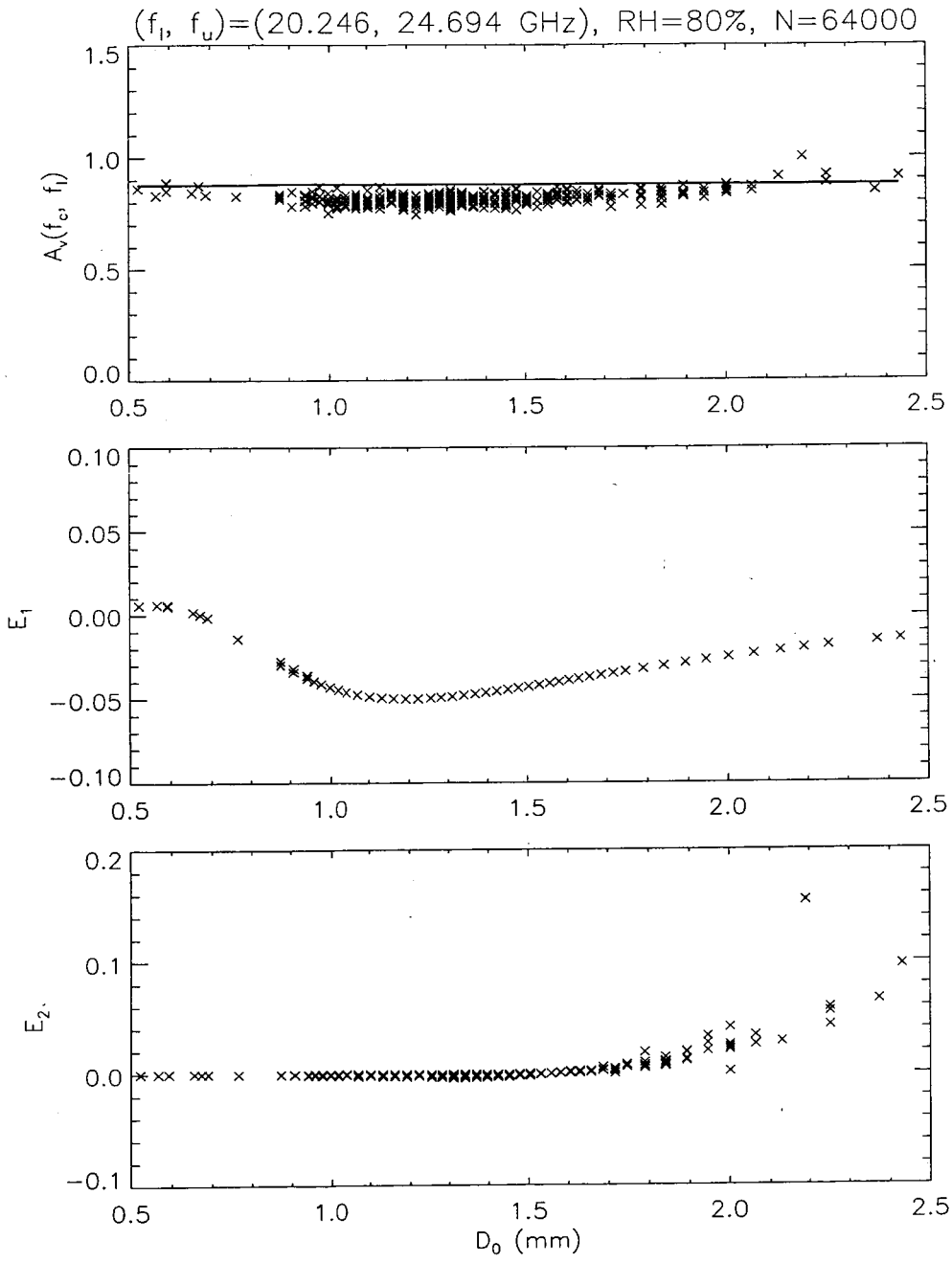

Fig.4. Top: Assumed (solid line) and estimated differential water vapor absorption (X) versus median raindrop diameter for a range gate near the surface; Center: Bias term E_1; Bottom: Bias term E_2 versus median drop diameter. γ=0.42.

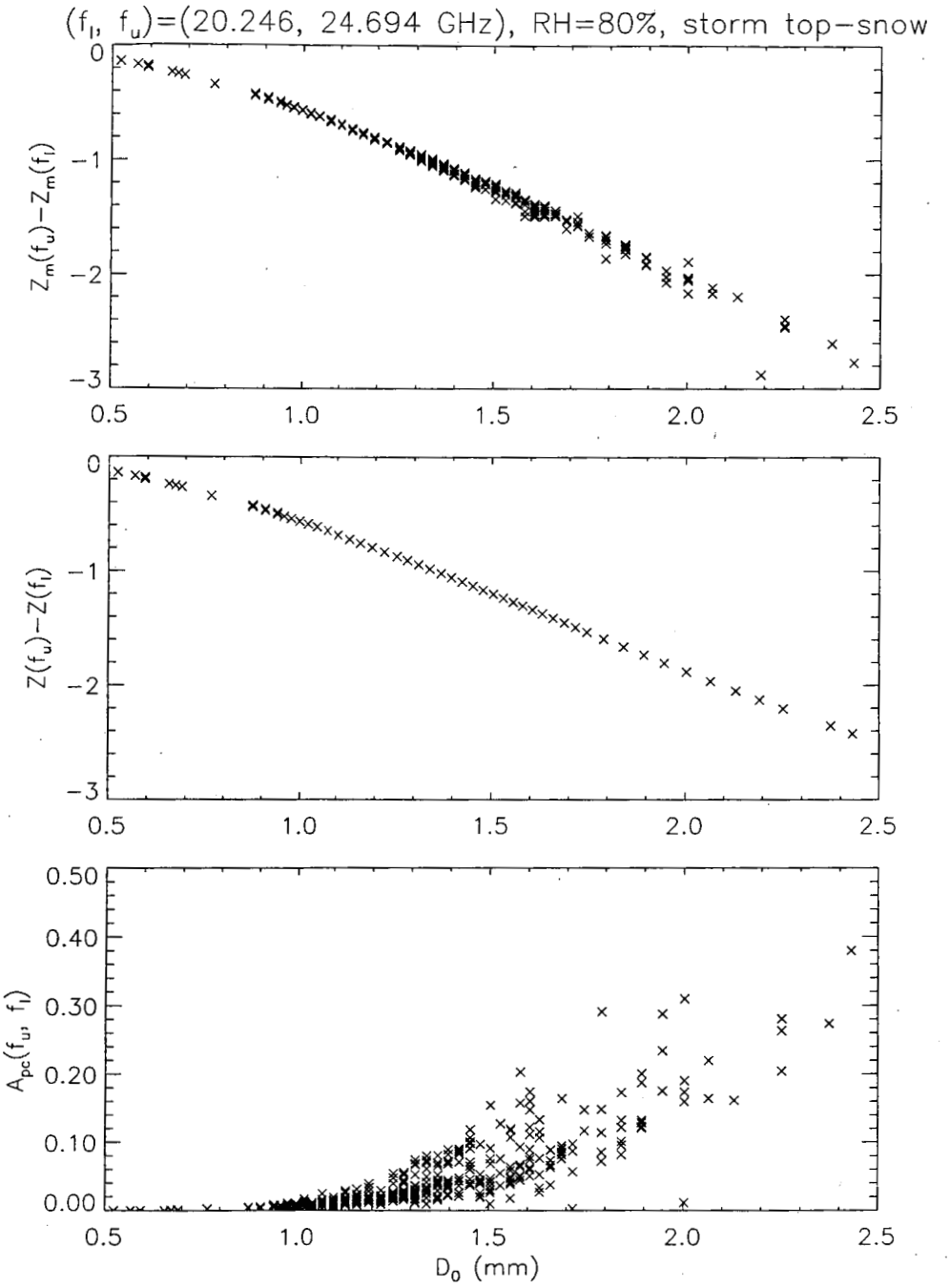

Fig.5. Measured (top) and 'actual' (center) differential reflectivity factor and differential path attenuation (bottom) for a range gate in the snow just above the melting layer versus median drop diameter of melted particles, D_0.

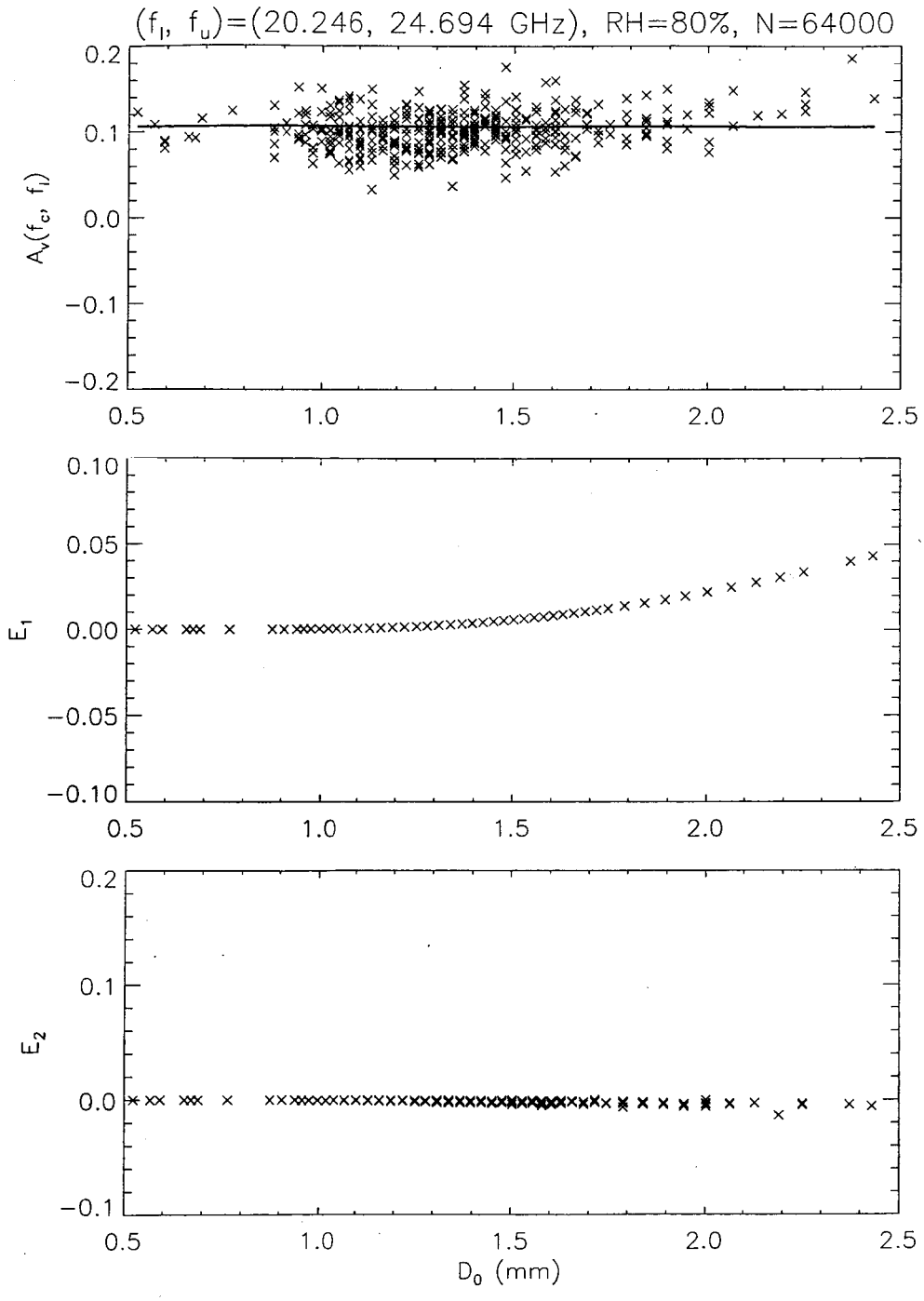

Fig.6. Top: Assumed (solid line) and estimated differential water vapor absorption (X) in snow versus median drop diameter of melted particles; Center: Bias term E_1; Bottom: Bias term E_2. γ=0.42.

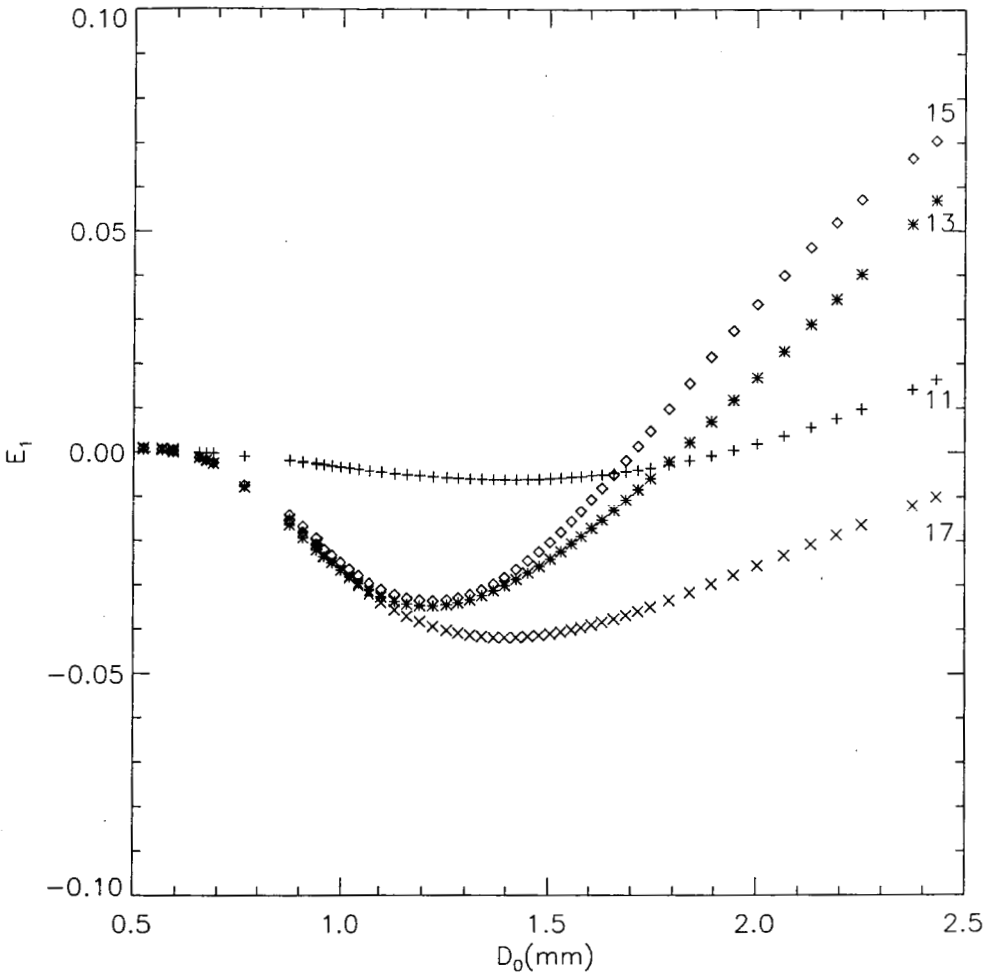

Fig.7. Bias term E_1 for four range gates (11, 13, 15, 17) within the melting layer versus median mass diameter of the equivolume raindrops.

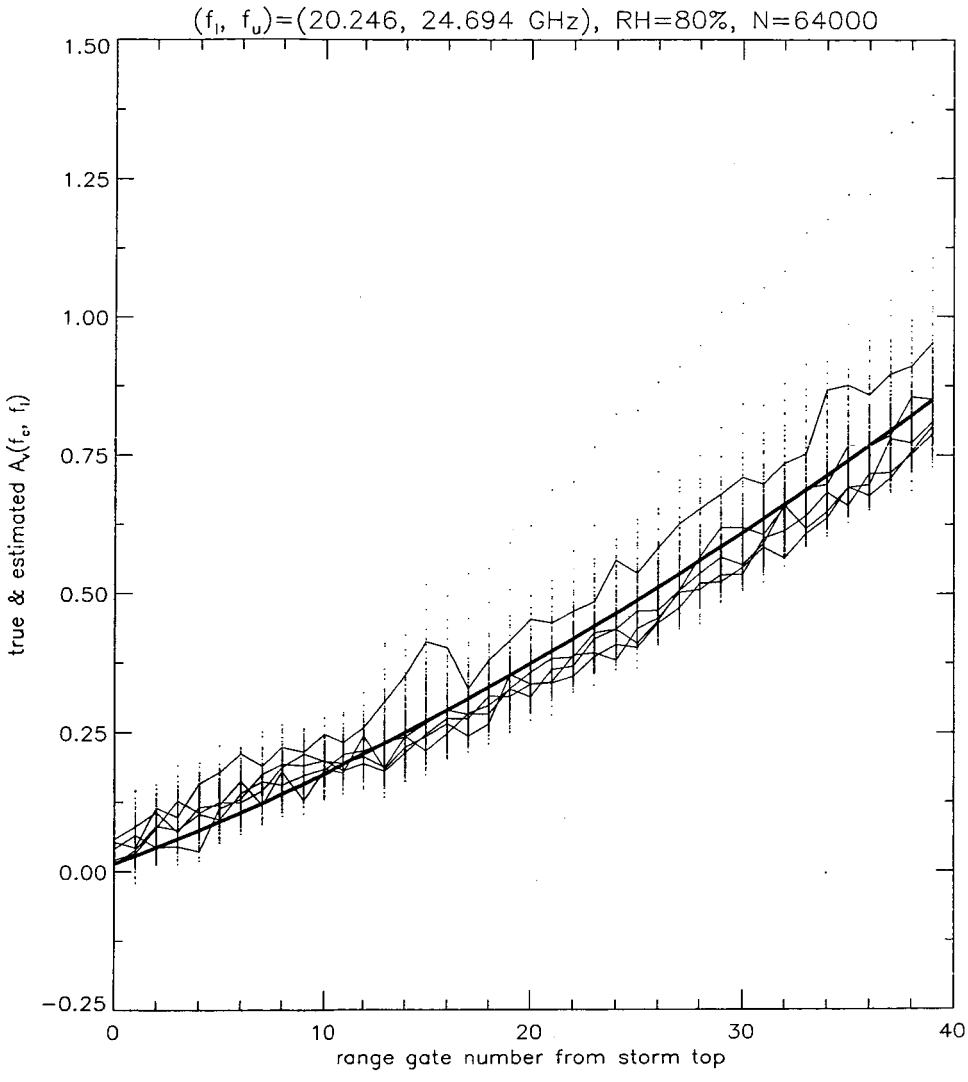

Fig.8. Five profiles of estimated differential water vapor absorption (thin lines) and assumed differential absorption (thick line) versus range gate number from storm top. The range gate spacing is 125 m. Results from all estimated profiles are indicated by the '+" symbol.

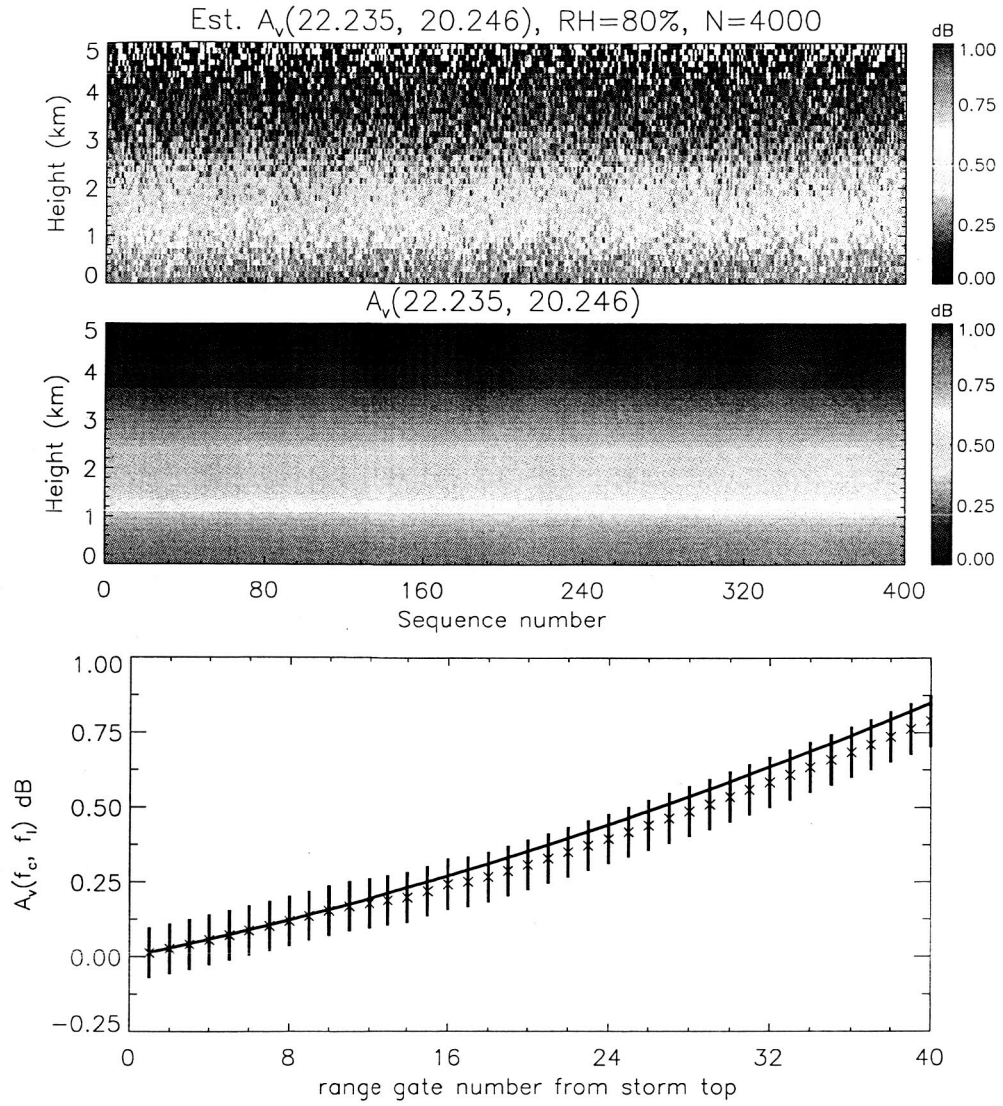

Fig.9. Estimated (top) and assumed (center) differential water vapor absorption; bottom: assumed (solid line) and the mean (X) and twice the standard deviation (vertical bars) of the estimates versus range gate number. A bandwidth of 20% is assumed with γ=0.42.

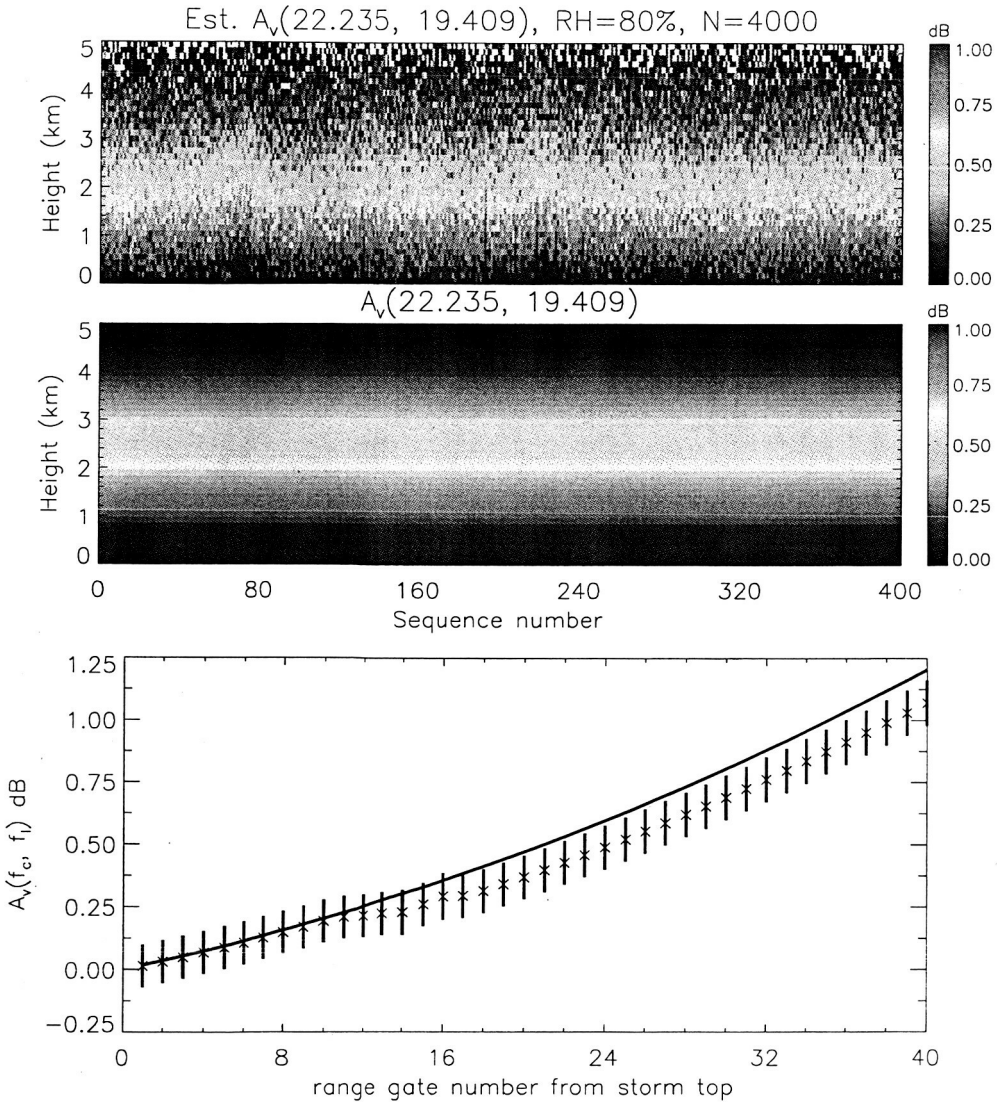

Fig.10. Same as Fig. 8 but for a bandwidth of 30%. γ=0.39.

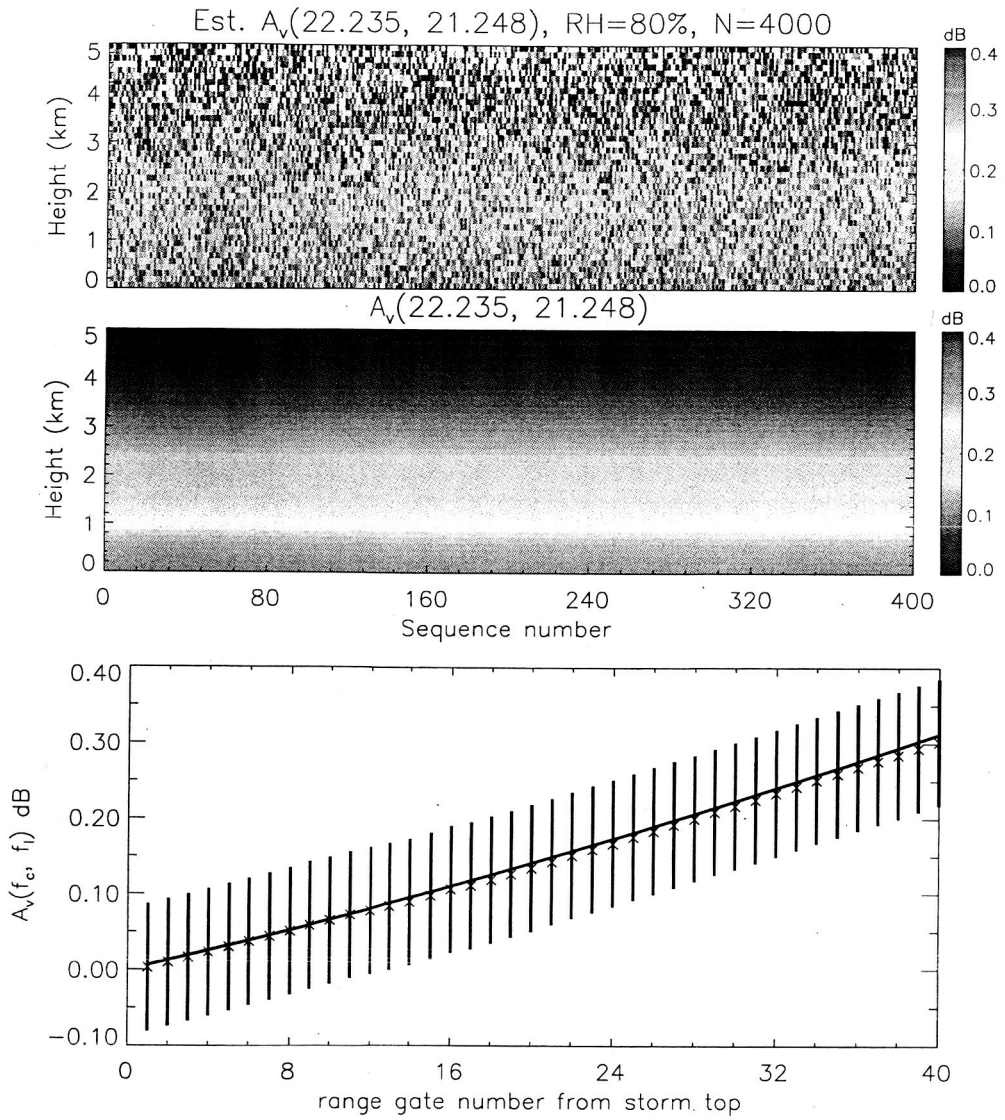

Fig.11. Same as Fig. 8 but for a bandwidth of 10%. γ=0.44.

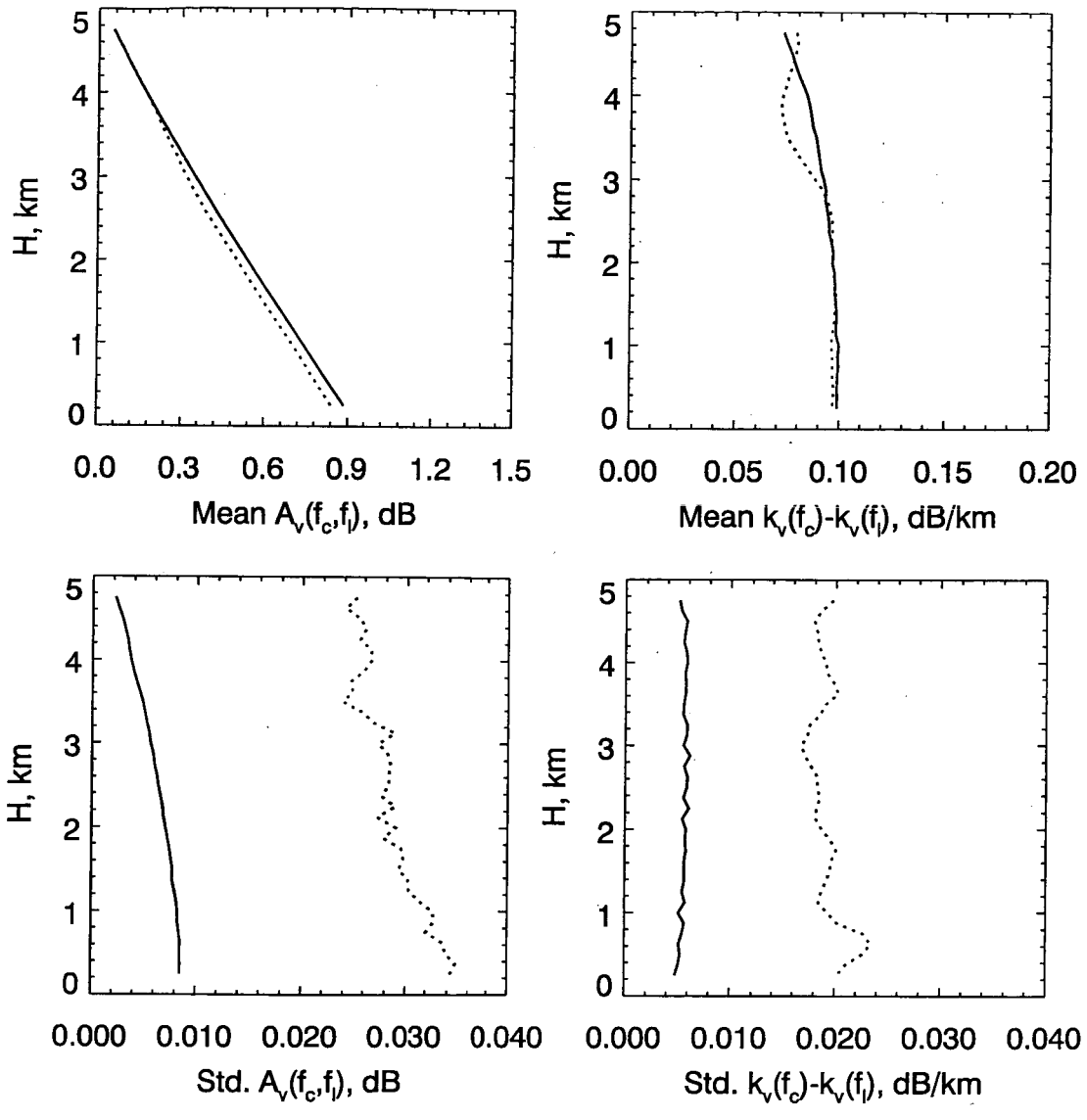

Fig.12. Top left: Mean profiles of estimated (dashed line) and assumed (solid) differential water vapor attenuation versus height. Top right: Mean profiles of estimated (dashed line) and assumed (solid) differential specific attenuation. Bottom left: Standard deviation of estimated (dashed line) and assumed (solid) differential water vapor attenuation. Bottom right: Standard deviation of estimated (dashed line) and assumed specific differential attenuation. n=16,000 and 20% bandwidth.

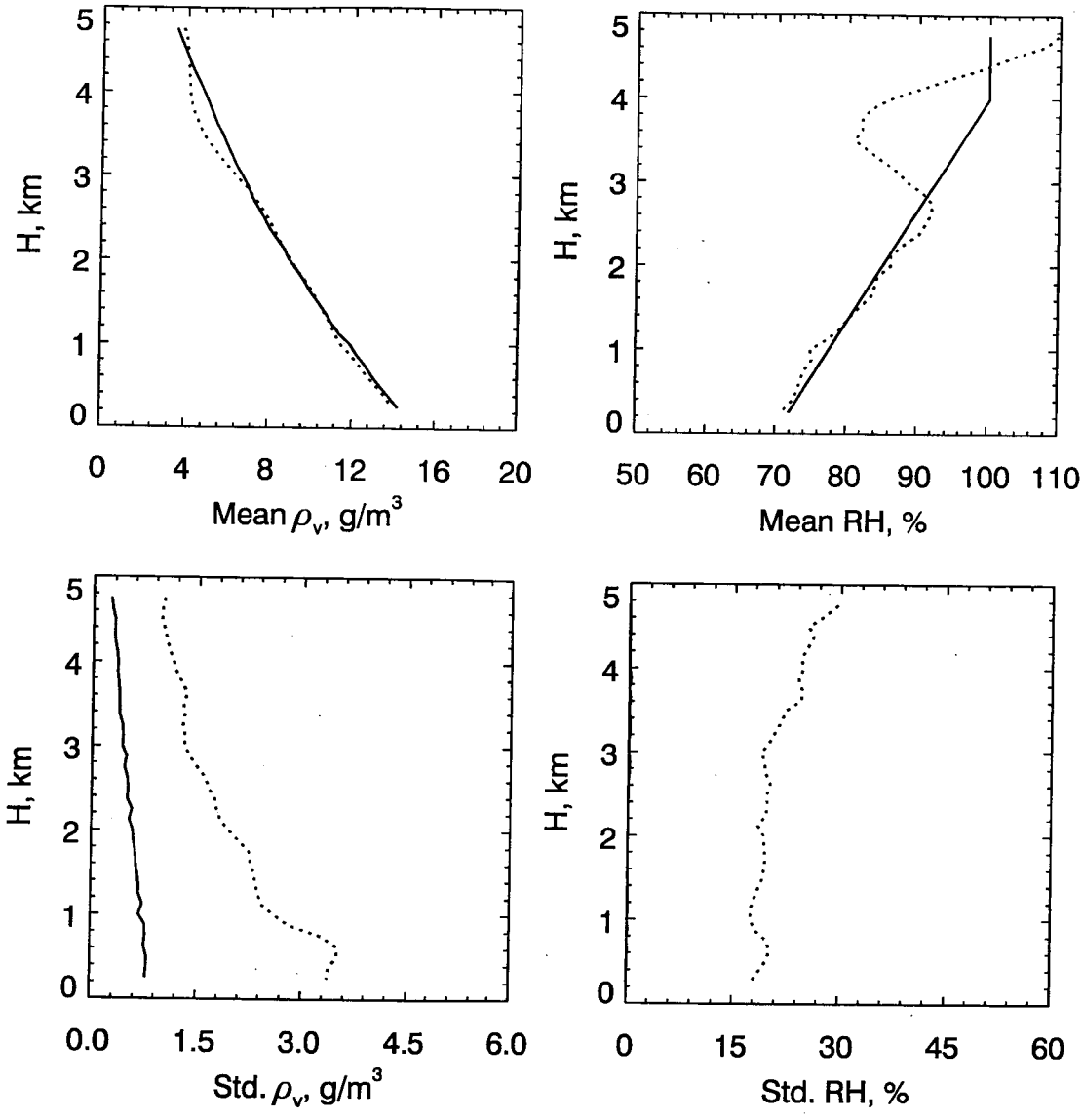

Fig.13. Top left: Mean profiles of estimated (dashed line) and assumed (solid) water vapor density versus height. Top right: Mean profiles of estimated (dashed line) and assumed (solid) relative humidity, RH. Bottom left: Standard deviation of estimated (dashed line) and assumed (solid) water vapor density. Bottom right: Standard deviation of estimated (dashed line) relative humidity. n=16,000 and 20% bandwidth.

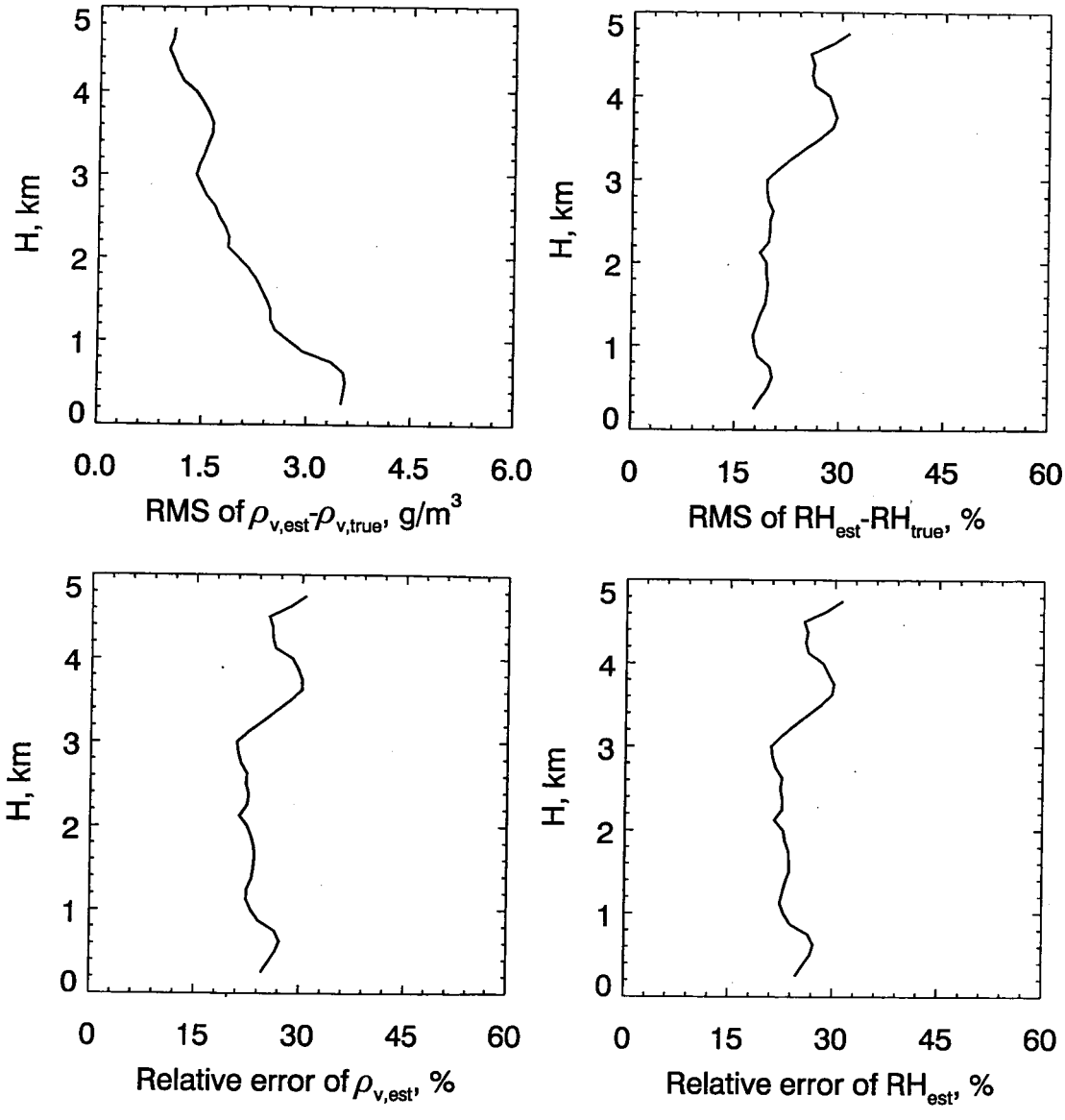

Fig.14. Top left: RMS error in estimate of water vapor density versus height. Top right: RMS error in estimate of relative humidity. Bottom left: Relative error in water vapor density estimate (RMS normalized by true value). Bottom right: Relative error in relative humidity estimate. n=16,000 and 20% bandwidth.